Remote Sensing of Environment 270 (2022) 112877

Contents lists available at ScienceDirect

Remote Sensing of Environment

journal homepage: www.elsevier.com/locate/rse

World Settlement Footprint 3D - A first three-dimensional survey of the global building stock

Thomas Esch *, Elisabeth Brzoska, Stefan Dech, Benjamin Leutner, Daniela Palacios-Lopez, Annekatrin Metz-Marconcini, Mattia Marconcini, Achim Roth, Julian Zeidler

German Aerospace Center (DLR), German Remote Sensing Data Center (DFD), Oberpfaffenhofen, D-82234 Weßling, Germany

ARTICLE INFO

Editor: Marie Weiss

Keywords:
Global
Building density
3D
Data fusion
TanDEM-X

ABSTRACT

Settlements, and in particular cities, are at the center of key future challenges related to global change and sustainable development. Widely used indicators to assess the efficiency and sustainability of settlement development are the compactness and density of the built-up area. However, at global scale, a temporally consistent and spatially detailed survey of the distribution and concentration of the building stock – meaning the total area and volume of buildings within a defined spatial unit or settlement, commonly referred to as building density – does not yet exist. To fill this data and knowledge gap, an approach was developed to map key characteristics of the world's building stock in a so far unprecedented level of spatial detail for every single settlement on our planet. The resulting World Settlement Footprint 3D dataset quantifies the fraction, total area, average height, and total volume of buildings for a measuring grid with 90 m cell size. The World Settlement Footprint 3D is generated using a modified version of the World Settlement Footprint human settlements mask derived from Sentinel-1 and Sentinel-2 satellite imagery at 10 m spatial resolution, in combination with 12 m digital elevation data and radar imagery collected by the TanDEM-X mission. The underlying, automated processing framework includes three basic workflows: one estimating the mean building height based on an analysis of height differences along potential building edges, a second module determining the building fraction and total building area within each 90 m cell, and a third part combining the height information and building area in order to determine the average height and total built-up volume at 90 m gridding. Optionally, a simple 3D building model (level of detail 1) can be generated for regions where data on the building footprints is available. A comprehensive validation campaign based on 3D building models obtained for 19 regions (~86,000 km^2) and street-view samples indicating the number of floors for >130,000 individual buildings in 15 additional cities documents that the novel World Settlement Footprint 3D data provides valuable and, for the first time, globally consistent information on key characteristics of the building stock in both, large urban agglomerations as well as small-scale rural settlements. Thus, the new dataset represents a promising baseline dataset for a wide range of previously impossible environmental, socioeconomic, and climatological studies worldwide.

1. Introduction

The rapid global urbanization is constantly progressing and two thirds of the world's population are expected to live in cities by 2050 (United Nations Department of Economic and Social Affairs Population Division, 2019). The unprecedented urban growth represents a megatrend that poses both challenges and opportunities, depending on how effectively this transformation is managed (d'Amour et al., 2017; Gozgor and Kablamaci, 2015; Grimm et al., 2008; He et al., 2014; Mahendra and Seto, 2019; Seto et al., 2012). Hence, the mapping and monitoring of settlements, and especially cities, is an essential component to develop a better understanding of the drivers and impacts of urbanization and to support sustainability and resilience strategies related to the built environment (Bakar and Cheen, 2013; Global Power Synergy Public Company, 2019; Grafakos et al., 2016; Lützkendorf and Balouktsi, 2017; United Nations Development Programme, 2016).

Here, Earth Observation (EO) has proven to be an effective instrument, in particular with respect to large-scale mappings of human settlements at continental and global scale (Esch et al., 2017; Florczyk et al., 2020; Marconcini et al., 2020; Román et al., 2018; Tiecke et al.,

* Corresponding author.
E-mail address: Thomas.Esch@dlr.de (T. Esch).

https://doi.org/10.1016/j.rse.2021.112877
Received 22 September 2021; Received in revised form 3 December 2021; Accepted 26 December 2021
Available online 8 January 2022

2017). However, considering the volumetric built-up density – which is a key parameter for estimating urban land use efficiency, population distribution, energy demand, or carbon emissions, – there are currently no spatially detailed datasets (< 100 m gridding) with global coverage.

From the point of view of sustainability, dense and compact settlements are considered to be favorable compared to low-density built-up areas (Bibri et al., 2020; Mahendra and Seto, 2019; Rosenthal and Strange, 2003). Thus, Brown De Colstoun et al. (2017) and Esch et al. (2018b, 2018c) aimed at providing first proxies for built-up densities at global scale by presenting worldwide datasets of the percent impervious surface within the built-up area. Hereby, regions with a higher imperviousness are considered to reflect a higher built-up density. Yet, for a more accurate and complete representation of the actual built-up density, an explicit assessment of the three-dimensional settlement structure is needed, most importantly in form of the area coverage and height of the buildings within the built-up area (often expressed as density or volume of the building stock). Furthermore, information about the three-dimensional settlement structure and built-up density are required to specify urban form and morphology, e.g. by means of compactness measures (Marshall et al., 2019) or a categorization into Local Climate Zones (Stewart and Oke, 2012). Such information can be employed to analyze the sustainability of urban areas (Williams, 2000) or to model the development of urban heat islands (Stewart et al., 2014). However, so far, the majority of existing datasets with three-dimensional settlement information is either restricted to analyses at city or regional level, or, if analyzed at large-scales, limited to comparably coarse spatial resolutions of >0.5–1.0 km.

Zhang et al. (2017) for example, analyze the horizontal and vertical urban growth of Guangzhou, China. They employ optical imagery at 30 m resolution to estimate mid-rise and taller buildings based on detected shadows. Mathews et al. (2019), on the other hand, use QuikSCAT data to calculate the built-up volume in nine U.S. cities. They find a strong correlation to built-up volume calculated using lidar data and, thus, highlight the strength of satellite-based radar backscatter to investigate urban growth. A combination of optical (Sentinel-2) and radar (TanDEM-X) data is applied by Geiß et al. (2019) to map built-up height and density in selected urban areas. In their work they examine major cities in Europe and present their estimations at a resolution of up to 200 m.

Looking at national or continental scale, existing datasets are sparse. Falcone (2016) derive height information from the NASA Shuttle Radar Topography Mission (SRTM) and calculate building heights by subtracting ground elevations points extracted from an external digital surface model (DSM). The height information is aggregated to census block groups, divided into six height categories, and exists for the whole area of the United States. Li et al. (2020) use a large set of different remote sensing data sources such as optical and radar imagery, a Normalized Difference Vegetation Index (NDVI) layer and roadmaps to train a random forest model that predicts the building footprint, building height, and building volume. Their estimations are generated at 1 km resolution and cover the US, Europe, and China. Frantz et al. (2021) train machine learning regression models. They use a combination of Sentinel-1A/B and Sentinel-2A/B time series to predict building height for entire Germany at 10 m resolution and highlight the benefits of the joint usage of optical and radar data. Further efforts in mapping vertical urban structures have been made by Clinton et al. (2018), Frolking et al. (2013), Lafarge et al. (2008), Mahendra and Seto (2019), Qin et al. (2015), Tison et al. (2007), and Xu et al. (2019).

The previously mentioned studies present innovative solutions, but so far, they are either limited to specific geographic regions (mainly cities, provinces, or countries in Europe, North America, or Asia), or their spatial resolution is still quite coarse (well above 100 m). Compared to existing work, the newly introduced World Settlement Footprint 3D (WSF 3D) framework is designed to resolve these limitations in terms of spatial coverage or low spatial resolution. This is achieved by fusing information from different global datasets, all of which already have high spatial resolution of at least 12 m. Moreover, the 3D building characteristics are directly extracted locally from global digital elevation data, instead of employing machine or deep learning models to estimate built-up heights from satellite imagery or other sources that do not contain direct height information (e.g., as suggested by Frantz et al., 2021; Li et al., 2020; Zhang et al., 2017).

To demonstrate the functionality and effectiveness of the new WSF-3D approach, information on the fraction, total area, average height, and total volume of the building stock are derived at a 90 m gridding for the entire land surface of the Earth. The technical implementation is detailed in Section 2 of this manuscript, followed by a specification of the various WSF 3D layers and the result of a comprehensive validation campaign in Section 3. Finally, Section 4 discusses the outcomes and in Section 5 the conclusions are drawn and an outlook on the future work is given.

In general, it is important to note that the research presented in this study aims at introducing the new methodology along with a comprehensive, quantitative validation of a first global WSF 3D dataset that has been processed with this novel approach. But, due to the given limitations on the maximum size of a manuscript, it is not possible to simultaneously include a geographic or qualitative analysis of global 3D building patterns or settlement characteristics within the scope of this publication. Nevertheless, this topic will be the subject of a corresponding follow-up study.

2. Methodology

The highly automated, modular processing framework used to derive the global WSF 3D reflects an advanced version of the methodology first presented by Esch et al. (2020). A general scheme of the workflow is illustrated in Fig. 1. Each of the three main WSF 3D processing modules (Building Height, Building Density, Built-up Volume) is described in detail in the related sub-Sections 2.1, 2.2, and 2.3.

The basic idea of the WSF 3D approach is to use the most up-to-date 2D global human settlement mask of the 10 m World Settlement Footprint 2019 (WSF 2019) introduced by Marconcini (2021) and then derive information on the 3D vertical structuring within the built-up area assigned by the WSF 2019 from the 12 m TanDEM-X Digital Elevation Model and the underlying 3 m Synthetic Aperture Radar (SAR) amplitude images (Zink et al., 2014). The amplitude images (TDX-AMP) used to produce the TanDEM-X elevation model (TDX-DEM) were collected between 2011 and 2013. TDX-DEM represents the most accurate elevation data currently available with global coverage.

For WSF 3D processing, the WSF 2019 settlement mask was supplemented with information about the percent impervious surface (IMP) within the assigned settlement area. The IMP is derived by integrating the global temporal maximum of the Normalized Difference Vegetation Index (NDVI) calculated from a collection of ~2.27 million Sentinel-2 (S2) granules with <60% cloud cover (level 2A, bottom of the atmosphere reflectance). Using the maximum NDVI and training data derived from Open Street Map (OSM, 2017), an ensemble of support vector regression modules is separately trained for each Köppen-Geiger climate zone to model the imperviousness for each 10 m settlement pixel of the WSF 2019 (Marconcini et al., 2020). Within the resulting WSF 2019 imperviousness layer (WSF-IMP), the road network is finally masked out based on related Open Street Map (OSM) data.

The technical framework to process and analyze the input datasets for WSF 3D production consists of three major modules. Within the settlement area designated by WSF-IMP, a first workflow identifies and measures height variations in the 12 m TDX-DEM which are most likely related to building edges (BE). These differences are then spatially aggregated at a 90 m grid, delivering an average building height (BH). All details related to the processing module are provided in Section 2.1. Subsequently, a second module (detailed in Section 2.2.) initially derives a binary building coverage layer (BC) at 12 m spatial resolution based on a joint analysis of WSF-IMP, TDX-AMP, and BE. Hereafter, the building fraction (BF) is calculated in the previously mentioned 90 m

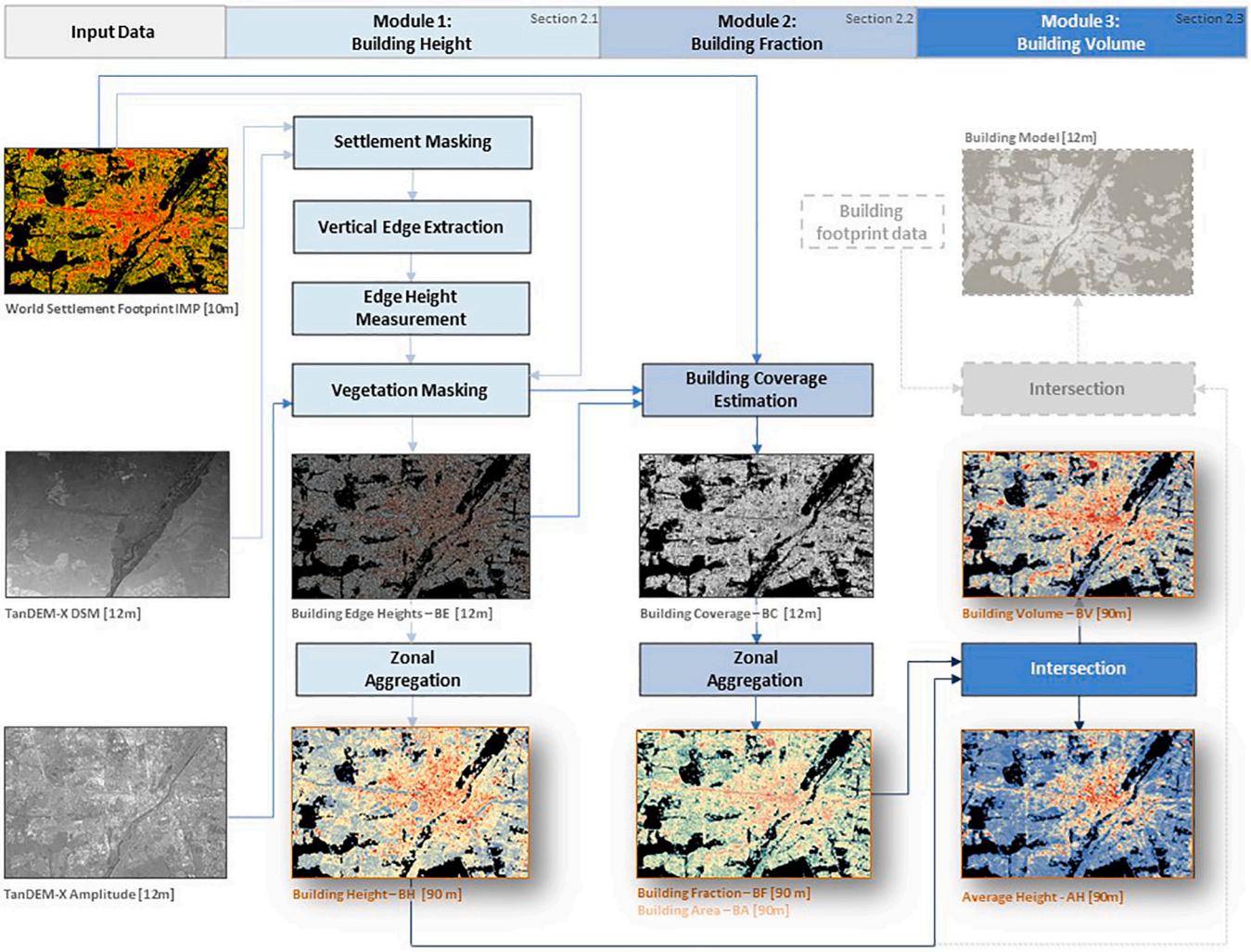

Fig. 1. Schematic view of the WSF 3D workflow implemented to estimate key 2D and 3D characteristics of the global building stock.

gridding by determining the percent building coverage within each 90 m cell based on BC. The information on BF is then used to define the total building area BA (in m^2) per 90 m grid cell (covering ~8100 m^2 at the equator). Finally, a third module combines the information of BH (outcome of module 1) and BF (outcome of module 2) to define the average height (AH) per grid cell (in m). For the AH calculation, all non-building pixels are counted with a height of 0 m. By multiplying the AH with the latitude dependent area of the 90 m grid cells, the AH is converted into the built-up volume (BUV), expressed in m^3. The third module is described in detail in Section 2.3.

The WSF 3D processing also includes the option to produce a high-resolution 3D building model (BMod) for regions where building outline data is available (e.g., from sources mentioned afore). In this case, BMod is generated by assigning all buildings provided by an external building raster or vector layer the average height as defined by BH.

In the context of the BC generation (module 2) it is important to note that the current solution – in contrast to the approach presented by Esch et al. (2020) – no longer foresees the integration of building outline layers. The main reasoning behind this adaptation is the fact that building outline data is still not consistently available for large parts of the world, although the corresponding databases are increasingly being built up, for instance in form an OSM building layer (available for many cities worldwide), Microsoft Building Footprints (Microsoft, 2018), Ecopia.AI/Maxar Technologies (Hallas, 2019), or the Open Buildings Dataset (Sirko et al., 2021). However, integrating regional building outline layers would finally restrict the cross-comparability and consistency of the global BF layer and WSF 3D, respectively, as the availability and characteristics of the input data to determine this essential parameter would ultimately still vary widely all over the world.

Finally, it is worth noting that the spatial generalization of the WSF 3D products to a gridding of 90 m is applied in order to compensate for spatial ambiguities resulting from the SAR-intrinsic layover effect at vertical structures which considerably handicap analyses at the original 12 m resolution (Esch et al., 2020). In the map-projected spatial domain, this layover leads to a spatial offset of local vertical structures (e.g., buildings) imaged by TDX-DEM and TDX-AMP with respect to the actual position of the identical structures or objects in BC and WSF-IMP (which are not subject to the specific distortion effects of the radar imaging principle). As a result, the edge or footprint of a building given by BC or WSF-IMP will most likely not directly overlay with the corresponding geometry of the same structure in TDX-DEM and TDX-AMP (the higher the building, the larger the spatial offset). Nevertheless, Esch et al. (2020) indicate that the effect of such local displacements can be reduced by spatially aggregating the input layers prior to the actual data and information fusion. The final decision to use exactly a 90 m gridding (e.g., instead of 60 m or 30 m) is subject to a German data distribution regulation (SatDSiG) which restricts the open provision of global products derived from TDX-DEM to a 90 m spacing (higher resolutions – such as achieved with the BMod extension – might only be provided for non-

crisis regions and countries on request).

2.1. Estimation of building heights

According to the methodology presented by Esch et al. (2020), the key step to derive building heights is based on the calculation of a normalized digital surface model (nDSM). However, first comprehensive analyses of the error patterns in the context of the systematic worldwide validation campaign (see Section 3) had shown that the step of detecting accurate and representative terrain ground points, which is needed for an accurate nDSM calculation, is prone to significant errors. In fact, it became apparent that in high-density built-up areas extending over steep slopes (e.g., imperviousness >75% and slope gradient >10%), and in settlements including rugged terrain features in the immediate vicinity of built-up structures (e.g., spikes, cliffs, bluffs, embarkments, gauges, sinks), the allocation of a sufficient number of correct ground points frequently fails. As a result, the terrain ground level interpolated from the identified ground points often does not accurately reflect the actual ground surface level. Consequently, the estimated (relative) above ground heights of local vertical structures differ significantly from the real situation. Here, three major types of errors were observed: most frequently, hill tops or small-scale topographic peaks and ridges located at hillsides are virtually cut due to a lack of ground points at or around their tops so that the heights of buildings located in the peak area are drastically overestimated (in fact, height differences resulting from the actual topographic situation are interpreted as building heights). Secondly, local cliffs or ramps in the terrain are not properly reflected in the modeled terrain ground level so that the corresponding rapid height variations along these linear structures are frequently interpreted as heights of the adjacent building structures (again, leading to an overestimation of the real building heights in these areas). Finally, in regions with very high building coverage (> 70–80%), often no ground points can be detected at all for extensive patches. In combination with a dynamic terrain, this effect leads to a considerable local overestimation of

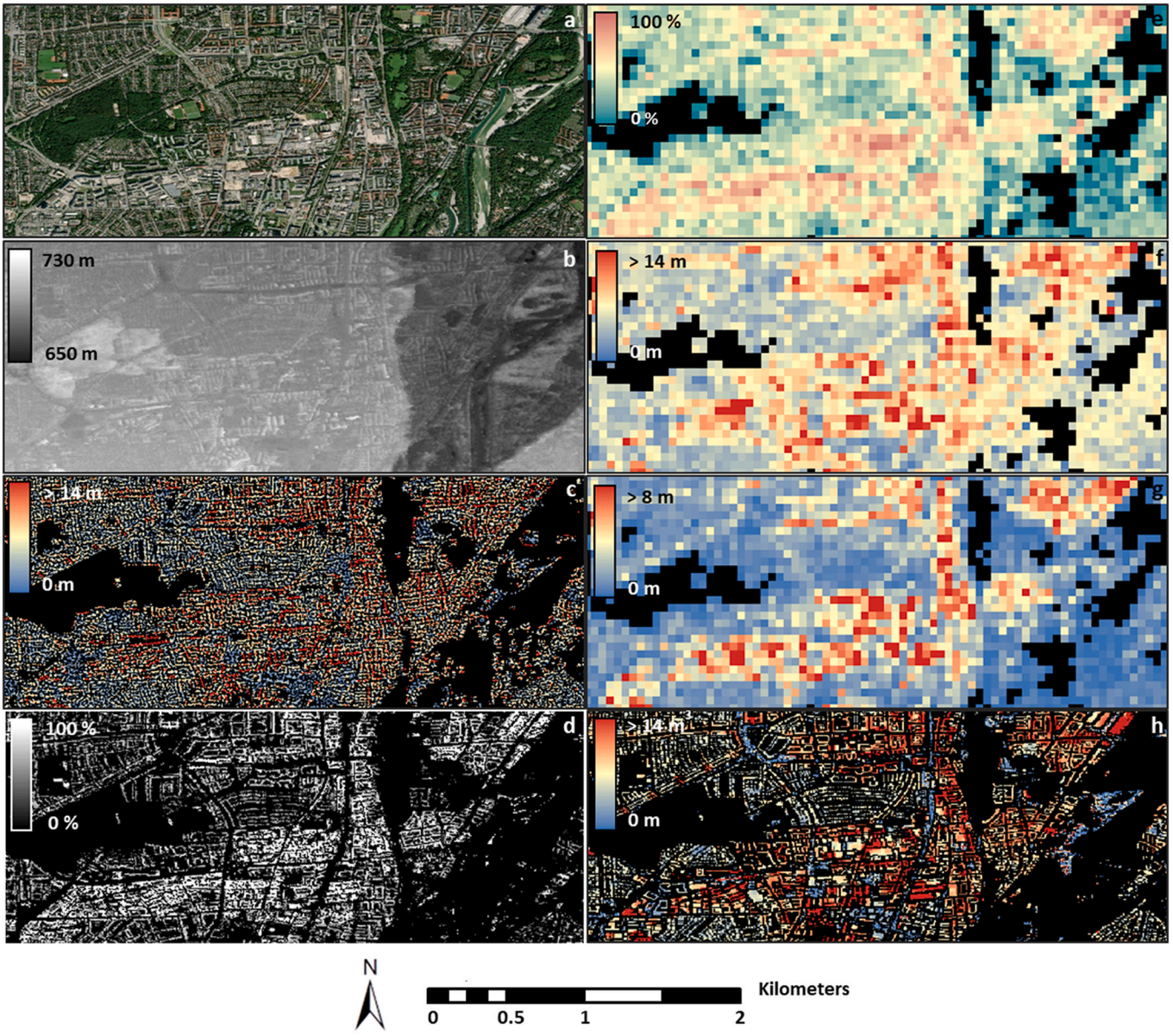

Fig. 2. Selected intermediate and final products of WSF 3D processing workflow. Optical view on the Obersendling district in Munich, Germany (a), 12 m TanDEM-X digital elevation model (b), extracted building edge heights BE (c), building coverage BC (d), and derived 90 m WSF 3D layers, including the building fraction BF (e), average building height BH (f), and average built-up height AH (g) provided at 90 m resolution, and the optional building model BMod (h) generated by combining OSM building footprints with the estimated building height BH.

building heights in built-up areas located at hill tops, and, in turn, large underestimation in case of built-up areas lying in sinks.

To avoid these negative effects, the original procedure of ground point detection, surface interpolation and nDSM calculation has now been replaced by an alternative approach. Instead of determining the building heights on the basis of a largely interpolated – and thus modeled – terrain (as in case of the former nDSM-based approach), the new method rather focuses on the analysis of height differences that actually occur in the immediate vicinity of assumed building structures in the original TDX-DEM. The central idea behind this approach is to avoid the often extreme errors in case of incorrectly interpolated terrain areas by only using real – meaning locally measurable – height values. Here, a key assumption is the hypothesis that buildings in the TDX-DEM always form a local height maximum, while the surrounding terrain surface represents the local minimum. Under this assumption, within built-up areas the height difference between local maxima and local minima (measured in a limited perimeter, e.g. 25 m) should correspond to the average height of the buildings in that area. A second assumption of the modified approach is that the outlines of building structures appear as distinct height edges in the TDX-DEM.

Considering these two assumptions, the new approach now focuses on the analysis of local height differences at supposedly vertical edges (VE) in the TDX-DEM within the settlement area. The height differences observed at VE – presumably belonging to building edges – are then measured and finally assigned to the closest building structure indicated by a building coverage layer that is described in detail in Section 2.2. In the TDX-DEM, VE usually occur as distinct punctual or linear local height variations along the outlines of buildings, walls, trees, or hedgerows (see Fig. 2b). To identify VE, one out of the four adapted versions of the Topographic Position Index (De Reu et al., 2013) originally employed by Esch et al. (2020) is used. The VE is defined in Eq. (1) and describes the relative height difference of a given pixel in TDX-DEM compared to its neighborhood defined by the median $\widetilde{X}$:

$$\mathrm{VE}\,[x,y] = \mathrm{DEM}[x,y] - \widetilde{X}_{i=x-2;j=y-2}^{x+2,y+2}\mathrm{DEM}[i,j] \quad (1)$$

A structure – or pixel in TDX-DEM – is considered as a candidate vertical edge in the TDX-DEM, if VE shows a value of >0.0, meaning the individual height value (above sea level) of a given pixel is higher than the median height (above sea level) in its immediate neighborhood (here, calculated within a 5 * 5 kernel).

Next, for all pixels where VE > 0.0 the local height variation H_E at the given edge is measured by calculating the difference between the actual TDX-DEM height value at the given pixel position and the minimum height value that occurs within a 5 * 5 pixels neighborhood (~ 25 m radius). However, in this step, the local slope of the terrain is to be considered as well, since any inclined terrain will bias the VE measurement within the analysis kernel. For example, in the case of a 6 m high house standing on a steep slope that has a height gradient of 2 m per 12 m horizontal distance (the latter corresponds to the edge length of a TDX-DEM pixel), the described approach will measure (within the perimeter of two pixels or ~ 25 m, respectively) a height difference of 10 m to the minimum at the position of the house edge (6 m height of the house plus an additional 4 m height difference due to the gradient of the terrain). Therefore, the natural slope of the terrain must be factored out when determining VE. This is done by normalizing the measured local edge height VE with the local slope of the terrain. To do so, the terrain slope is estimated by first removing all local maxima and vertical edges – here defined as TDX-DEM pixels where VE > 0.0. Subsequently, the created local gaps in the TDX-DEM elevation data are filled by means of a four-direction conic search distance weighting available in the GDAL (GDAL/OGR contributors, 2020) software.

The resulting edge-smoothed TDX-DEM can now be expected to primarily reflect the height differences which are induced by the local terrain slope because all local height structures have been removed and flattened, respectively. To get the slope-corrected edge height H_{ES}, the slope-induced local height difference H_S is measured based on the edge-smoothed version of TDX-DEM and then subtracted from the height difference observed at the same position in the original TDX-DEM dataset as described in Eq. (2). Again, using the example of the house on the slope, this would mean that the height difference of 4 m induced through the terrain (= H_S) is subtracted from the height difference of 10 m actually measured at the edge of the house in the original TDX-DEM (= H_E). The resulting slope-corrected height difference (= H_{ES}) is thus 6 m (which corresponds to the actual height of the building).

In this context, comprehensive empirical tests have revealed that the local above ground heights derived from the TDX-DEM (even when synthetically optimized by manual editing procedures) still show a systematic underestimation bias of the real building edge heights which increases with the actual height of the structure. This phenomenon can in part be attributed to the layover effect mentioned before, but is also related to the fact that due to the 12 m pixel spacing, the actual height differences between the building and the surrounding ground have already been levelled to some degree in the elevation model as a result of the mixed pixel problem (meaning one TDX-DEM pixel might cover part of a building and part of the surrounding terrain, leading to a mixed height value and a smoothed height edge at the building outline, respectively).

Hence, the raw values resulting from the subtraction of H_S and H_E are finally multiplied by an empirically determined, height-dependent correction factor f_H which increases from a value of 1.5 at 15 m up to 2.5 for H_{ES} values >25 m:

$$\mathrm{H_{ES}}[x,y] = (\mathrm{H_E}[x,y] - \mathrm{H_S}[x,y])^{*}f_H = \quad (2)$$

$$\left[\left(\mathrm{DEM}[i,j] - MIN_{i=x-2;j=y-2}^{x+2,y+2}\mathrm{DEM}[i,j]\right) - \left(\mathrm{DEM_S}[i,j] - MIN_{i=x-2;j=y-2}^{x+2,y+2}\mathrm{DEM_S}[i,j]\right)\right]^{*}f_H$$

Once the final heights H_{ES} of all edges VE are defined, those edges related to vegetation (e.g., trees, hedges) have to be removed in order to generate the final building edge height layer BE. The related vegetation masking is based on the imperviousness information provided by WSF-IMP. Here, a H_{ES} pixel is masked out as vegetation in BE if WSF-IMP <10 (meaning that more than 90% of the pixel area is covered by vegetation). Generally, it is important to note that comprehensive empirical tests with an alternative IMP layer generated on the basis of 30 m Landsat data collected in 2012 (meaning the exact time of the TDX-DEM data acquisition) clearly indicated the superiority of the IMP information derived from the 10 m Sentinel-2 data, although the imagery was collected between 2017 and 2019. The reason is that the WSF 2019 settlement mask, although including additional settlement areas that arose between 2012 and 2019, still shows a higher overall accuracy compared to the settlement mask derived from the rather coarse 30 m Landsat imagery. Moreover, the 2019 imperviousness estimation at 10 m led to a much more precise, and thus efficient, masking of local urban green spaces compared to the results obtained from the 30 m Landsat data.

In a final step, the average building height (BH) is estimated at a 90

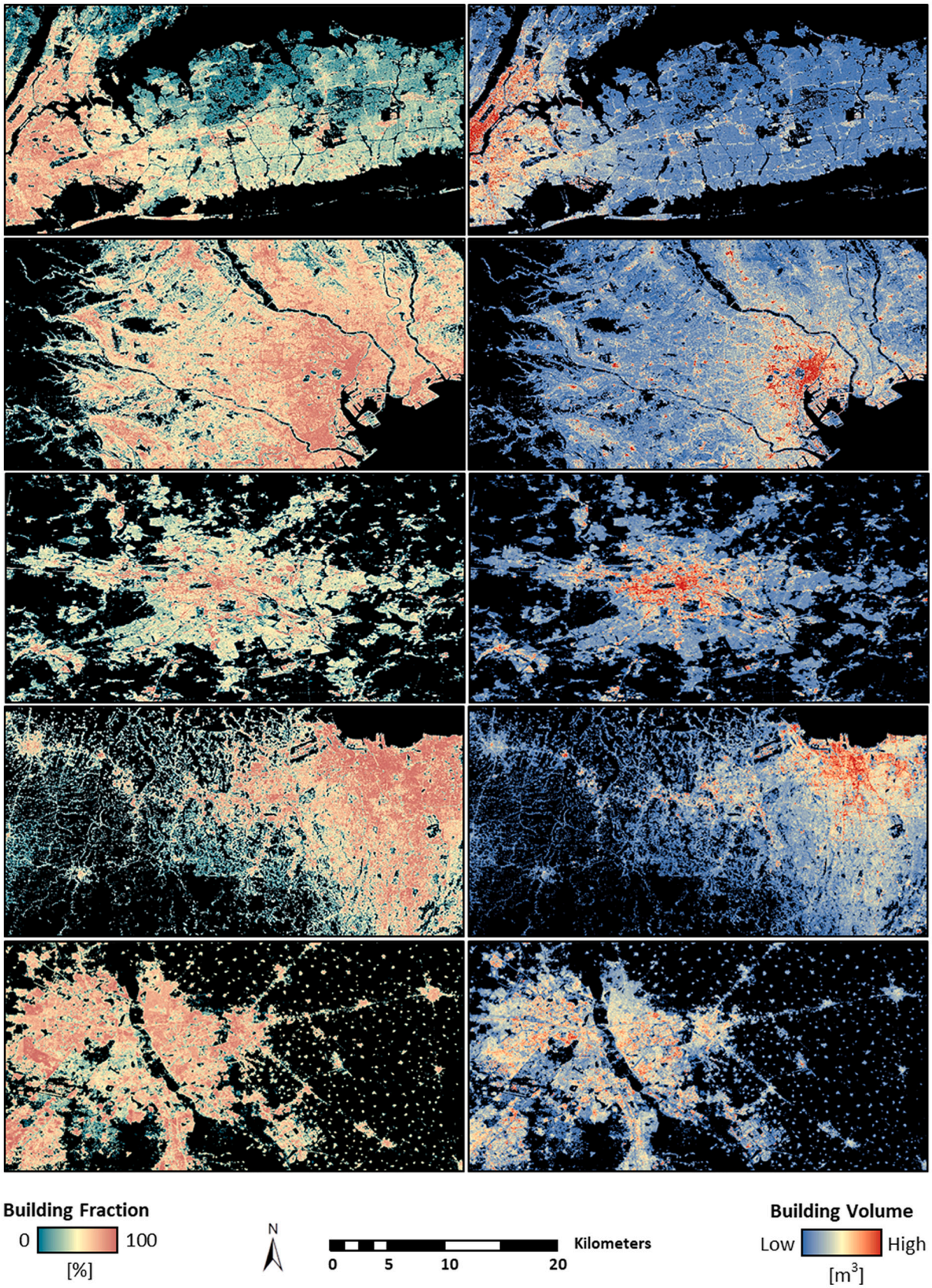

Fig. 3. Examples of WSF 3D 90 m building fraction (BF) and total building volume (BV) estimated – from top to bottom – for New York (USA), Tokyo (JPN), Berlin (DEU), Jakarta (IDN), and New Delhi (IND).

m gridding (see Fig. 1, Fig. 2, and Fig. 3) by calculating the mean from all heights provided by the building edge height layer BE as defined in Eq. (3):

$$\mathrm{BH}_{90\mathrm{m}}\,[\mathrm{x},\mathrm{y}] = \sum_{i=x^*7}^{x^*7+6}\sum_{j=y^*7}^{y^*7+6}\mathrm{BE}[i,\mathrm{j}] \Bigg/ \sum_{i=x^*7}^{x^*7+6}\sum_{=y^*7}^{y^*7+6}\begin{cases}1, \mathrm{BE}[i,\mathrm{j}]. > 0\\ 0, \mathrm{BE}[i,\mathrm{j}] \le 0\end{cases} \tag{3}$$

As mentioned already, the aggregation to a 90 m gridding is also subject to the SatDSiG which currently restricts the open provision of global TDX-DEM elevation data.

2.2. Calculation of building fraction

To identify and delineate buildings and building structures, a building coverage layer (BC) at 12 m spatial resolution is generated at first (see Fig. 1). The key input to BC is the WSF-IMP. However, since impervious areas not only include buildings, but also represent flat impermeable surfaces such as paved courtyards, squares, or driveways, the WSF-IMP layer is corrected by a masking operation on the basis of two auxiliary layers L_{AMP} and L_{BE} (please note that roads had already been masked out during WSF-IMP production with OSM and thus do not have to be removed in this step again).

L_{AMP} is derived from the radar backscattering characteristics of TDX-AMP for all regions lying within a settlement area as defined by WSF-IMP. A pixel in L_{AMP} is supposed to represent a potential vertical building structure if two evaluation criteria δ_{Amp} and δ_{Tex} defined in Eqs. (4)–(8) are met in the form that $\delta_{Amp} > 1.0$ and $\delta_{Tex} > 0.3$. Generally, these two criteria indicate that TDX-AMP pixels show a relatively higher backscatter value than their neighborhood, which is a typical characteristic for vertical objects such as buildings or trees (e.g., due to double-bounce effect, direct backscatter, or steep incidence angle). The parameter δ_{Amp} (Eq. (6)) represents the maximum of the ratios (Eq. (5)) of the TDX-AMP to the focal mean (Eq. (4)) for focal window sizes of 3, 5, 7, 9, and 11. These kernel sizes correspond to distances of ~12 m - 60 m around the center pixel and comprehensive tests had shown that within these distances the distinctness of building structures (in terms of their relatively higher values in TDX-AMP) can be effectively determined.

The parameter δ_{Tex} (Eq. (8)) describes the ratio of the focal standard deviation (Eq. (7)) of TDX-AMP and the focal mean (Eq. (4)) for a window size of 11.

$$mA[N,x,y] = \frac{1}{N^*N}\sum_{i=x-N/2}^{x+N/2}\sum_{j=y-N/2}^{y+N/2}\mathrm{AMP[i,j]} \tag{4}$$

$$rA[N,x,y] = AMP[x,y]/mA[N,x,y] \tag{5}$$

$$\delta_{Amp}[\mathrm{x},\mathrm{y}] = Max(\, rA[3,x,y]\,, rA[5,x,y]\,, rA[7,x,y]\,, rA[9,x,y]\,, rA[11,x,y]\,) \tag{6}$$

$$sdA[N,x,y] = \sqrt{\frac{1}{N^*N}\sum_{i=x-N/2}^{x+N/2}\sum_{j=y-N/2}^{y+N/2}(\mathrm{AMP[i,j]} - mA[N,i,j])^2} \tag{7}$$

$$\delta_{\mathrm{Tex}} = SdA[11,x,y]/mA[11,x,y] \tag{8}$$

More detailed information on the background and effectiveness of the two parameters δ_{Amp} and δ_{Tex} is provided in Esch et al. (2020). Since the potential vertical edges identified with the help of δ_{Amp} and δ_{Tex} can still include both buildings, but also vertical vegetation elements (e.g., trees, hedges), all pixels dominated by vegetation are masked out based on the WSF-IMP layer following the procedure already described in the context of the H_{ES} and BE calculation in Section 2.1.

The second auxiliary layer contributing to the WSF-IMP masking is L_{BE}, which indicates the presence of buildings where the previously generated building edge height dataset BE shows a height of >3.0 m. Three meters correspond to the usual height of one floor of a building.

$$\mathrm{BF}_{90\mathrm{m}}\,[\mathrm{x},\mathrm{y}] = \sum_{i=x^*7}^{x^*7+6}\sum_{j=y^*7}^{y^*7+6}BC[i,j] \Big/ 49 \tag{9}$$

To form the final building coverage layer BC at 12 m (see Fig. 2 and Fig. 3), all pixels of WSF-IMP having a value >0.0 and either featuring a $\delta_{Amp} > 1.0$ and $\delta_{Tex} > 0.3$, or showing a BE >3.0, are kept, whereas these WSF-IMP pixels that do not meet the criteria are assigned a value of 0.0. In a last processing step, the building fraction (BF) is then determined at 90 m gridding by calculating the mean of all 49 (7 * 7 kernel) 12 m BC pixels (with values ranging from 0 to 100%) within each 90 m cell (see Fig. 1 and Fig. 3) according to Eq. (9):

The underlying BF (given in %) is additionally provided in form of the total building area BA (given in m^2), as described in Eq. (10). BA results from the exact pixel size, which depends on the x- and y-resolution of the tile and its latitude.

$$\mathrm{BA}_{90\mathrm{m}}\,[\mathrm{x},\mathrm{y}] = \mathrm{BF}_{90\mathrm{m}}\,[\mathrm{x},\mathrm{y}]^*Area[x,y] \tag{10}$$

2.3. Computation of average built-up height and building volume

In the last step of the WSF 3D processing, the estimated building heights provided by BH are merged with the building fraction defined by BF in order to describe the building density (see Fig. 1). Here, two representations are implemented: the average height (AH) and the related total building volume (BV), as detailed in Eq. (11) and Eq. (12):

$$\mathrm{AH}_{90\mathrm{m}}\,[\mathrm{x},\mathrm{y}] = \mathrm{BH}_{90\mathrm{m}}\,[\mathrm{x},\mathrm{y}]^*\mathrm{BF}_{90\mathrm{m}}\,[\mathrm{x},\mathrm{y}]/100 \tag{11}$$

$$\mathrm{BV}_{90\mathrm{m}}\,[\mathrm{x},\mathrm{y}] = \mathrm{AH}_{90\mathrm{m}}\,[\mathrm{x},\mathrm{y}]^*Area_{90\mathrm{m}}[x,y] \tag{12}$$

To determine AH, BH is multiplied by BF. Here it is worth noting that all 12 m BC pixels within the given 90 m cell are counted with the building height BH assigned to this cell and all remaining (non-building) pixels are considered with a height of 0 m. By multiplying AH with the $\mathrm{Area}_{90\mathrm{m}}$ (~ 8100 m^2 at the equator), the total building volume (BV), expressed in m^3, is derived. AH and BV can be considered as a descriptor for the building density since they combine the information on the building height with the given building footprint area within a given area – here, the 90 m cells (Fig. 2 and Fig. 3).

In addition to the standard 90 m WSF 3D layers, the processing framework also offers the option to generate a simple 3D building model (BMod) with level of detail 1.0 (block model). This optional layer is derived by assigning the average building height provided by BH to all buildings defined by the 12 m BC raster layer (BModr), or alternatively, vector data defining the building outlines (BModv), such as available regionally from several sources (Hallas, 2019; OSM, 2017). In case of BModv, the proportional area of the building polygon with respect to the 90 m cells is considered if a building extends over several 90 m cells of BH. Although the 90 m BH information does not allow for a precise per-building height assignment, the example given in Fig. 4 clearly illustrates that the simple block model can still add valuable information to a 2D building footprint layer.

Regarding the processing infrastructure for the WSF 3D production, a fully operational and data-driven system has been deployed in the secured TanDEM-X production environment. There, all 26,453 TDX-DEM tiles (and same number for TDX-AMP tiles) were jointly analyzed with the WSF-IMP by means of DLR proprietary software implemented in C++, in combination with GDAL. The WSF 3D processor as such is installed on a Sun X 4640 machine with eight CPUs/64Cores at 2.6 GHz and 256 GB RAM. With that infrastructure a global run of the entire WSF 3D processing workflow from scratch required approx. 20 days. The collection of ~2.27 M S2 granules used to generate the WSF-IMP layer was processed at the Google Earth Engine (GEE) and then transferred to the WSF 3D processing facility.

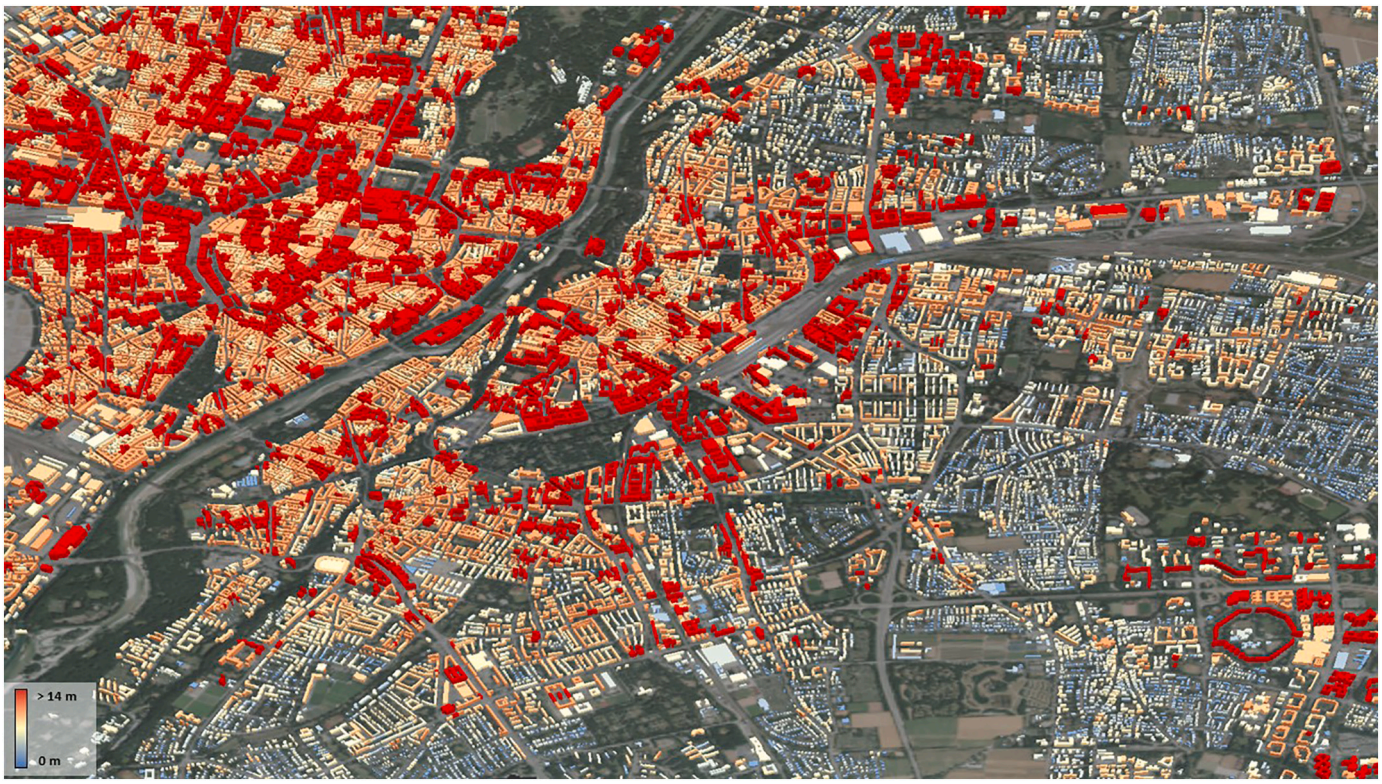

Fig. 4. WSF 3D building model. Exemplary perspective view on a building model (vector version BModv) generated for the Munich area, Germany, by combining building polygons provided by OSM with the heights assigned by the WSF 3D building height layer BH.

Table 1
WSF 3D product specification. Main product characteristics of the five standard WSF 3D products generated at global scale, along with a description of the optional building model.

Product name	Abbrev.	Spatial Resolution	Unit	Coverage	File Name (example)
Average Building Height	BH	90 m	m	Global	WSF3D_V01_e011_n49_e012_n48_BuildingHeight_90m
Building Fraction	BF	90 m	%	Global	WSF3D_V01_e011_n49_e012_n48_BuildingFraction_90m
Total Building Area	BA	90 m	m^2	Global	WSF3D_V01_e011_n49_e012_n48_BuildingArea_90m
Average Height	AH	90 m	m	Global	WSF3D_V01_e011_n49_e012_n48_AverageHeight_90m
Total Building Volume	BV	90 m	m^3	Global	WSF3D_V01_e011_n49_e012_n48_BuildingVolume_90m
Building Model(r/v)	BModr	12 m	m	Regional	WSF3D_V01_e011_n49_e012_n48_BuildingModelr_12m
	BModv	vector	–	Regional	WSF3D_V01_e011_n49_e012_n48_BuildingModelv

3. Results

3.1. Product description

The WSF 3D standard layers (Table 1) are provided in the format of Lempel-Ziv-Welch (LZW)-compressed GeoTiff files, with each file – or image tile – covering an area of 1 * 1° geographical lat/lon at a geometric resolution of 2.8 arcsec (~ 90 m at the equator). Following the system established by the TDX-DEM mission, the latitude resolution is decreased in multiple steps when moving towards the poles to compensate for the reduced circumference of the Earth.

In this specification, one global coverage of WSF 3D products finally consists of 18,634 files in total (only including tiles that contain at least one settlement pixel as defined by WSF). The (regional) vector version of the WSF 3D building model (BModv) is delivered in form of a shapefile. The heights of BH, AH, and BModr are provided in m with a gain factor of 0.1 for storage optimization (Int16). The area of BA is indicated in m^2, BV is given in m^3, and BF shows 1-% steps with values ranging from 0 to 100.

The naming convention of each tile follows a structure that specifies the product family, processing version, location (upper-left and lower-right corner coordinates of the tile), product name, and spatial resolution. In addition, a virtual mosaic file (.vrt) is provided to facilitate an effective visualization of the global layers at once (e.g., on GIS platforms).

3.2. Validation

The strategy for the technical validation of the global WSF 3D layers includes, on the one hand, a validation campaign based on VHR 3D building models obtained for 19 globally distributed regions (Section 3.2.1). This validation based on a comparison to building models is supplemented by a second evaluation that uses ground-truth sample points derived via crowd-sourcing from 75,724 street-view images collected in 15 additional cities worldwide and indicating the number of floors for a total of 130,459 individual buildings (Section 3.2.2).

3.2.1. Comparison to area-wide reference data

The first validation campaign is based on a comprehensive quantitative accuracy assessment of the WSF 3D layers using very high-resolution building models (< 50 cm, level of detail 1) assessed for 19 regions worldwide and covering a total of 85,878 km^2 (see Table 2). The

Table 2
Validation results for WSF 3D building fraction (BF), building height (BH), and building volume (BV). The error statistics defined for the related 90 m products BuildingFraction, AverageHeight, and BuildingVolume are provided in form of mean error (ME), mean absolute error (MAE), and root mean square error (RMSE), derived by means of quantitative comparison to reference building models. The accuracies reported for BuildingFraction (BF) apply to the total building area (BA, BuildingArea product) and the ones for the BuildingVolume to the built-up height AverageHeight (AH) because the latter represent a conversion of the units of measurement from one sphere into another.

Reference site	BF_{NoBL}			BH_{NoBL}			BV_{NoBL}		
	ME	*MAE*	*RMSE*	*ME*	*MAE*	*RMSE*	*ME*	*MAE*	*RMSE*
Almaty (KAZ)	8	12.1	16.19	−1.77	3.03	5.29	−21	5265	8375
Amsterdam (NLD)	−0.91	9	13.3	0.15	2.78	5.57	−826	6581	14,254
Cartagena (COL)	0.29	6.52	8.98	−0.55	0.83	1.07	−1015	2416	3379
Christchurch (NZL)	6.23	10.48	15.09	−0.55	1.57	2.48	668	3174	5441
Dongying (CHN)	10.54	17.29	23.62	−5.47	5.9	9.62	−4241	9689	15,572
Indianapolis (USA)	−1.15	6.98	10.24	−0.37	1.81	3.02	−919	2720	7291
Karachi (PAK)	0.22	11.83	15.7	−3.97	4.99	7.67	−8122	12,355	20,316
Kigali (RWA)	12.53	13.06	16.37	0.2	0.99	1.53	3797	4169	5825
Lipa (PHL)	0.84	6.83	9.44	0.71	1.25	1.72	1114	2620	4965
Munich (DEU)	−2.48	7.48	10.39	−4.25	4.58	6.61	−6416	7189	11,521
Nairobi (KEN)	11.94	17.03	23.79	−2.01	3.35	6.75	1561	8679	15,026
New York (USA)	2.75	9.42	13.24	0.98	3.09	6.62	830	7186	17,977
Niamey (NER)	12.99	13.6	16.74	−1.07	1.3	1.77	1795	2913	3968
Seoul (KOR)	−2.72	10.39	14.23	−13.14	13.61	21.1	−22,779	24,257	39,483
Tanuan (PHL)	−6.48	8.56	10.89	0.53	1.29	1.82	−1010	2259	4023
Vienna (AUT)	−0.96	8.36	12.61	0.07	2.36	3.75	−1151	4877	8943
Washington (USA)	2.79	8.99	12.54	−2.27	3.27	5.24	−1716	6433	13,791
Bavaria (DEU)	0.93	6.79	10.24	−2.91	3.11	4.01	−5174	5873	13,760
Gyeonggi (KOR)	2.74	9.93	14.19	−8.04	8.47	19.05	−9728	12,027	22,905
Mean	**3.06**	**10.24**	**14.09**	**−2.30**	**3.56**	**6.04**	**−2808**	**6878**	**12,464**

related datasets predominantly cover urban areas and their immediate rural vicinity. In this context it is important to note that the selection of these validation sites was constrained by the limited availability of open and free reference datasets suitable for this purpose. Nevertheless, the final list of spots given in Table 2 shows that the study sites cover a diverse spectrum of cultural and geographical regions. The validation sites are predominantly characterized by urban settlements, but especially two building models available for all settlements in the German federal state of Bavaria and the South Korean province Gyeonggi include a large number and variety of rural villages and hamlets as well. To compile the final reference layers for the WSF 3D product validation, the information of the reference building models was spatially aggregated to the 90 m gridding of the standard WSF 3D products. Next, each resulting 90 m reference dataset was virtually subdivided into 500 * 500 pixels tiles from which one quarter was randomly selected to form the basis for an empirical definition and tuning of optimal parameter settings during product development. The other three quarters of the cells were used for the actual statistical validation of the WSF-3D layers.

Considering the sequential production process of the WSF 3D (see Fig. 1), three basic components can be expected to fundamentally influence the accuracy of the final layers: the precision of the WSF 2019 mask which is used to assign the settlement area, the quality of the building mask BC from which the building fraction BF is derived, and the accuracy of the estimated building heights provided by the BH layer.

As the performance and accuracy of the WSF has already been determined in detail at global scale, reference can be made at this point to the corresponding work of Marconcini et al. (2020), which refers to the World Settlement Footprint 2015 dataset. The outcome of that study reported accuracies of 83–89% (Kappa 0.55–0.78), depending on the semantic and related structural definition of the settlement area. First results of a just recently conducted validation campaign for the WSF 2019 (Marconcini, 2021) based on 779,976 globally distributed validation samples document a comparable an overall accuracy of 84% and a Kappa of 0.65 (a related scientific publication will be finished and submitted in the next weeks by Marconcini et al.).

The building coverage BC is used to derive the building fraction (BF) and building area (BA) within each 90 m grid cell. Moreover, BC affects the quality of the measured average height of the built-up structures (AH) and built-up volume (BV). Finally, the optional 12 m raster building model (BMod) is based on the building geometries defined by BC as well. To validate BC, the building fractions and building areas calculated at the 90 m WSF 3D gridding are compared against the corresponding values derived from the building geometries provided by the reference building models available for the 19 globally distributed validation sites. The outcomes of this quantitative validation – expressed in form of mean error (ME), mean absolute error (MAE), and root mean square error (RMSE) – are summarized in Table 2.

Considering the building fraction BF, the accuracy metrics indicate a trend towards overestimation. In total, 13 out of 19 test sites show a ME >0, with the span of values ranging from −6.48% for Tanuan to 12.99% for Niamey. The MAE ranges between 6.52% for Cartagena and 17.29% for Dongying and shows an average MAE over all test sites of 10.24%.

The test sites with the highest ME (> 10%) simultaneously tend to have the highest mean absolute error (MAE) values (> 10%), such as Nairobi, Kigali, Niamey, or Dongying. All these sites have in common that in between buildings they often exhibit extensive areas of bare soil (e.g., dust roads, sidewalks, or fallow land without vegetation cover). Moreover, the roofs frequently have materials similar to the substrate surrounding the buildings. In these cases, the BC analysis tends to overestimate the percentage of building coverage due to the spectral similarity between uncovered soil and buildings on the one hand, and the 12 m resolution of the BC dataset on the other hand (mixed-pixel problem). The latter leads to the effect that buildings are often represented in form of mixed pixels so that the building outline is blurred and therefore slightly overexaggerated if the surrounding ground looks similar.

The precision of the building height estimation is validated by comparing the WSF 3D building height product (BH) with the average building heights resulting from the aggregation of the reference building models to the identical 90 m gridding (see Table 2). The results show a mean error (ME) ranging from 13.14 m for Seoul to 0.98 m for New York and indicate an underestimation of height for 13 out of 19 test sites. The MAE lies between 0.85 m for Cartagena and 13.61 m for Seoul.

As already reported by Esch et al. (2020), the validation shows that the height estimation error increases with the actual height of the buildings. While for buildings with an average height of a few meters (e.g., 1–3 stories) the ME is comparatively accurate, the error increases systematically with rising building height. From heights of >30 m, the

Table 3
Validation of WSF 3D building height (BH) information according to the categorization used for the mapping of Local Climate Zones.

Reference site	BH_{NoBL}						
	Precision			*Recall*			*Overall Accuracy*
	3–10 m	10–25 m	> 25 m	3–10 m	10–25 m	> 25 m	
Almaty (KAZ)	0.74	0.742	0.284	0.962	0.303	0.109	0.737
Amsterdam (NLD)	0.855	0.55	0.21	0.874	0.51	0.214	0.779
Cartagena (COL)	1	–	–	1	–	–	1
Christchurch (NZL)	0.961	0.517		0.985	0.296		0.947
Dongying (CHN)	0.429	0.752	0.764	0.982	0.219	0.059	0.483
Indianapolis (USA)	0.961	0.526	0.368	0.99	0.255	0.093	0.951
Karachi (PAK)	0.644	0.692	0.292	0.965	0.23	0.047	0.647
Kigali (RWA)	0.984	0.394	–	0.993	0.232	–	0.977
Lipa (PHL)	0.98	0.318	–	0.98	0.318	–	0.961
Munich (DEU)	0.67	0.838	0.694	0.982	0.369	0.069	0.701
Nairobi (KEN)	0.761	0.664	0.143	0.973	0.198	0.006	0.753
New York (USA)	0.924	0.426	0.447	0.886	0.555	0.312	0.821
Niamey (NER)	0.994	0.417	–	0.998	0.169	–	0.992
Seoul (KOR)	0.174	0.413	0.869	0.935	0.182	0.105	0.26
Tanuan (PHL)	0.985	0.409	–	0.983	0.429	–	0.969
Vienna (AUT)	0.855	0.698	0.15	0.898	0.605	0.212	0.812
Washington (USA)	0.862	0.659	0.693	0.972	0.413	0.312	0.834
Bavaria (DEU)	0.923	0.585	0.264	0.991	0.164	0.055	0.916
Gyeonggi (KOR)	0.478	0.415	0.774	0.959	0.14	0.057	0.473
Mean	**0.799**	**0.556**	**0.458**	**0.964**	**0.310**	**0.127**	**0.790**

capability to accurately estimate the real building height is very limited due to the SAR-intrinsic layover effect. In addition, the error pattern for these very high buildings is usually quite noisy as well, due to statistical effects that result from the usually quite small population of high-rise buildings.

An alternative way to present the building height is the vertical aggregation of the estimated heights into categories with a defined height range. By doing so, the height estimation errors are compensated to a certain degree since they now rather have an effect around the boundaries of the defined height categories. As an example, Table 3 reports accuracies resulting from a transformation of the building height layer BH into three vertical categories defined according to a scheme used for the established Local Climate Zones mapping (Stewart and Oke, 2012): 3–10 m, 10–25 m, and > 25 m.

Considering the ability of the model to correctly predict a certain category (precision), it can be seen that category 1 (3–10 m) is best predicted with an average precision over all test sites of 0.799, followed by category 2 (10–25 m) depicting a precision of 0.556 and category 3 (> 25 m) with 0.458. However, the values among the test sites can vary considerably. Especially for category 1, 12 test sites achieved a value of >0.85. Test sites with higher average reference building heights tend to show a higher precision for category 2 and 3 (e.g., Seoul, Dongying, and Munich). Looking at the amount of actual data that was correctly predicted by the model (recall), a pattern similar to the behavior of the precision can be noted: category 1 (3–10 m) shows the highest values with an average recall of 0.964, followed by category 2 (10–25 m) with 0.31, and category 3 (> 25 m) with 0.127. The overall accuracies range from 0.99 for Niamey (NER) to 0.260 for Seoul (KOR), with a mean overall accuracy for the 19 test sites of 0.79.

The statistical accuracy of the WSF 3D Building Volume (BV) product – and therewith also for the Average Height (AH) which forms the basis for the conversion of the average height (AH) per 90 m cell into a volume by multiplying AH with the fixed area of each cell – is presented in Table 2 as well. Here it is important to note that the quality of Average Height and Building Volume, respectively, is basically defined by the accuracies of the two input products Building Fraction (BF) and Building Height (BH) from which they are derived (see Eq. (11) and Eq. (12)).

The ME for BV ranges between −22,789 m^3 for Seoul and 3797 m^3 for Kigali and shows a trend to underestimate the building volume for the presented test sites. The MAE lies between 2259 m^3 for Tanuan and 24,257 m^3 for Seoul. The magnitude of the error follows the average building height of a test site, meaning the higher the average building height of a city is, the higher the error bars observed. For Seoul, a city showing a large number of very high buildings, the average reference building height is 22.09 m. At the same time, the city depicts by far the highest error for BV, here in form of a considerable underestimation. A similar behavior is observed for Karachi (mean reference BH 11.83 m) or Munich (mean reference BH 11.06 m). In turn, Tanuan (mean reference BH 3.01 m) or Cartagena (mean reference BH 3.57 m) show the highest accuracies for the estimated BV. To develop a better understanding of the error values of the Building Volume product, one can assume that a large single-family house with six to seven rooms, a floor space of around 120 m^2, and a living space of around 220 m^2, equals a building volume of around 1000 m^3 (Röthlisberger, 1999).

While the statistics described above give an idea of the absolute deviations between the WSF 3D products and the ground truth data, they provide only limited information on the relative differences. Hence, Fig. 5 presents exemplary cross-sections through the cities of Indianapolis and Munich. Thereby, the building fraction (BF), building height (BH), and building volume (BV) are plotted for the WSF 3D and the reference data along a representative spatial profile. Although the underestimation of height and volume is confirmed in absolute terms, the profiles nevertheless show that the relative trends or trajectories of the height distribution are well reflected. Additionally, the plots confirm the good fit of the building fraction estimation, as already reported quantitatively in Table 2.

3.2.2. *Comparison to local crowdsourcing data*

The validation based on a comparison to building models is supplemented by a second evaluation that uses ground-truth sample points derived via crowd-sourcing from 75,724 street-view images collected in 15 cities worldwide (see Table 4) and indicating the number of floors for a total of 130,459 individual buildings. The labelling was conducted by students of the Resilience Academy (https://resilienceacademy.ac.tz). The sources of the street view data included, on the one hand, crowd-sourced geotagged photos, hosted by Mapillary (https://www.mapillary.com) and acquired all around the world by volunteers using simple tools like smartphones or action cameras. Downsampled versions of those images (up to 2048 pixels in width) are available for download and can be used under the Creative Commons Attribution-ShareAlike 4.0 International License (CC BY-SA 4.0). On the other hand, high-resolution, 360 degrees panoramas with associated accurate geotags

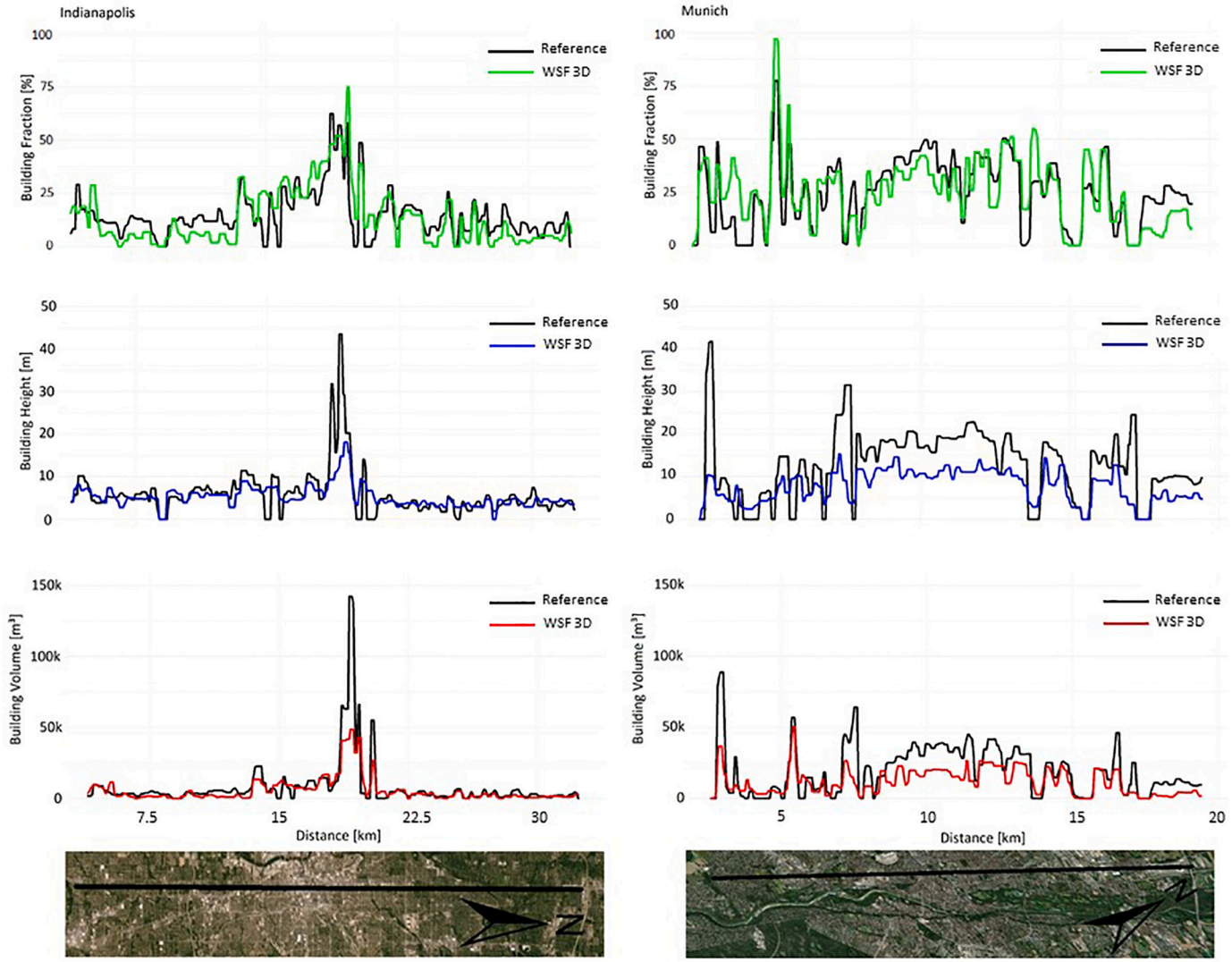

Fig. 5. Cross-sections indicating the building fraction, height, and volume along a transect through the cities of Indianapolis and Munich. The profile for Indianapolis covers a distance of 32.5 km and runs through the city center. For Munich, the profile shows a length of 18.8 km and the city center area is crossed as well.

Table 4
Evaluation of WSF 3D BuildingHeight product (BH) based on reference points indicating the number of floors which have been converted in an estimated building height.

Reference site	Deviation between BH_{NoBL} and reference height [m]		
	ME	*MAE*	*RMSE*
Abidjan (CIV)	−3.7	4.07	5.26
Aizuwakamatsu (JPN)	−2.44	3.04	4.42
Dar es Salaam (TZA)	−3.26	4.42	7.21
Denver (USA)	−2.88	4.3	7.16
Detroit (USA)	−0.21	2.31	3.84
Huston (USA)	−0.94	3.03	5.5
Lagos (NGA)	−4.55	5.12	7.92
Marrakesh (MAR)	−4.54	5.59	7.07
Miami (USA)	−4.24	5.76	9.74
Padang (IDN)	0.22	1.51	2.02
Port Alfred (ZAF)	−0.51	1.03	1.51
Rabat (MAR)	−3.13	4.43	5.61
Santa Cruz de Tenerife (ESP)	−3.68	5.01	7.2
Sevastopol (UKR/RUS)	−4.54	5.51	8.56
Vilnius (BLR)	−9.51	9.51	11.96
Mean	**−3.19**	**4.31**	**6.33**

and orientation information collected by the Swiss company MindEarth during two field campaigns carried out in 2019 and 2020, are used. The corresponding collections cover most of the streets in the neighborhood of Riviéra Palmeraie in Abidjan (IC).

To evaluate the WSF 3D, the labelled information on the number of building floors is first converted into a building height by assuming an average floor height of 3 m. The resulting reference building heights are then quantitatively compared to the building height provided by the WSF 3D Building Height product (BH) for the 90 m cell in which the reference point is located. The outcome of this comparison is documented in Table 4.

Generally, the results confirm the tendency of a systematic underestimation (as reported in Table 2 as well). Considering the ME, the values range from −9.51 m for Vilnius to 0.22 m for Padang. On average, the MAE shows slightly higher values than presented in Table 2, ranging from 1.03 m for Port Alfred to values of up to 9.51 m for Vilnius. The higher error margins compared to the outcomes presented in Table 2 might arise from the fact that the labelling campaign was focused on the assignment of the number of floors to a single building, whereas the WSF 3D BuildingHeight (BH) layer is estimated via a spatial integration over 90 * 90 m. In addition, the assumed height of 3 m per floor may actually differ from the real situation depending on the local context. However, the results basically confirm the validation results achieved on the basis

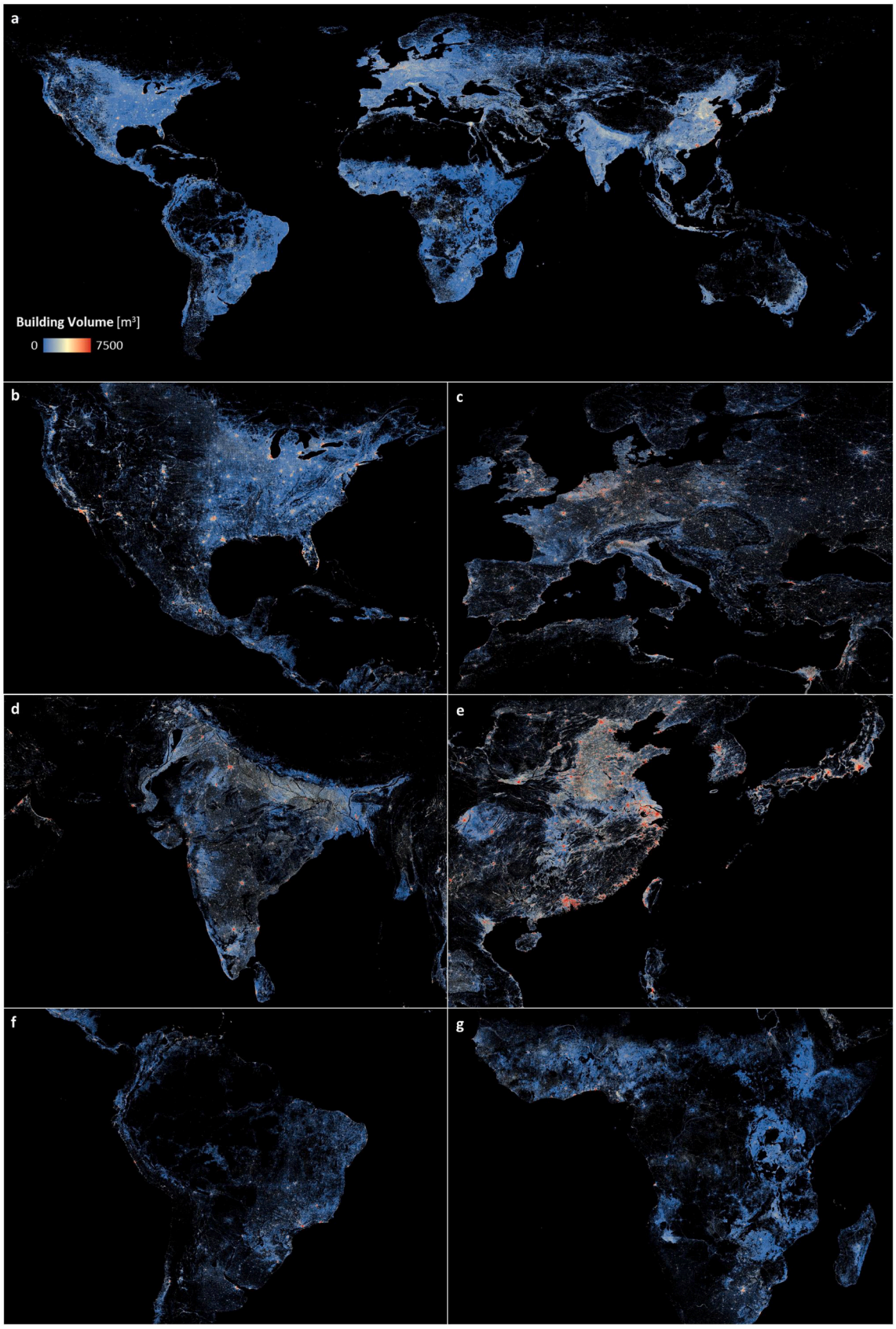

Fig. 6. Distribution of building volumes at global scale (a), and for North America (b), Europe (c), India (d), East Asia (e), South America (f), and Africa (g).

of a comparison to the reference building models (see Table 2) and indicate a solid building height estimation with an average MAE of ~1.5 floors over all test sites.

4. Discussion

The outcomes of the validation campaign generally indicate a high potential of the new WSF 3D dataset to support a broad spectrum of applications that require information about the horizontal and vertical settlement extent, the compactness, and density of the settlement and building structure, or other morphologic characteristics of the built environment. Here, the WSF 3D layers can provide new empirical evidence on key structural features of the building stock, at a level of detail which is so far unique for a dataset in a consistent worldwide coverage. Fig. 6, for instance, illustrates the pattern of building volumes at global and continental scale as provided by the BuildingVolume (BV) product. Initial figures on the global building stock derived from the WSF 3D data show a total worldwide building area of 291,577 km^2, a mean building height of 5.55 m, and a total volume of 1,632 km^3 (the mean building volume is 6.92 km^3). Looking at the individual continents, the following picture emerges: North America has a building area of 42,904 km^2, a mean building height of 5.34 m, and a building volume of 227.30 km^3 (mean volume: 9.88 km^3), South America of 15,394 km^2, 5.10 m, and 77.63 km^3 (mean volume: 6.47 km^3), Europe of 61,994 km^2, 6.08 m, and 358.53 km^3 (mean volume: 7.63 km^3), Africa of 37,210 km^2, 4.77 m, and 176.32 km^3 (mean volume: 3.27 km^3), Asia of 130,064 km^2, 6.17 m, and 770.84 km^3 (mean volume: 16.40 km^3), and Oceania of 3,285 km^2, 5.09 m, and 17.28 km^3 (mean volume: 0.96 km^3). A more detailed global analysis of all building characteristics is planned as part of a future publication.

Considering the usage of the WSF 3D data it is worth noting that due to the specifics of the WSF mask used to outline human settlements, the WSF 3D does not consistently include very small settlement patches such as hamlets, huts, or shacks (Marconcini et al., 2020). Regarding the height estimation, the WSF 3D validation has shown the ability to accurately determine the height of buildings higher than ~25–30 m (~ 8–10 floors) is very limited. Therefore, it has to be taken into consideration that the tendency to underestimate – or, in effect, cap – the heights of high-rise buildings in the WSF 3D data increasingly impacts the accuracy of outcomes and findings in regions with a large proportion of corresponding high-rise building structures. As a result, the building height and building volume are most likely underestimated in high-rise areas (see Fig. 5). However, the example of the Local Climate Zones (LCZ) illustrates that the WSF 3D data can still be valuable and accurate (see Table 3) when working with height categories that include one class which covers all high-rise buildings (in the case of LCZ, the class >25 m which is used besides the categories 3–10 m and 10–25 m).

Moreover, it is important to note that the error bars grow with rising spatial detail of the analysis units – e.g., as seen when comparing the MAE (reflecting the deviations between modeling results and ground truth at the pixel level) with the ME (in effect, reflecting the aggregated accuracy resulting from spatial averaging – here, at the level of an entire city) where positive and negative deviations equal out to a certain degree. Therefore, WSF 3D-based analyses at the level of building blocks, districts, or entire settlements can generally be considered more significant than very local evaluations at the level of single pixels or individual buildings. For such spatially aggregated units the observed mean error lies in the dimension of one story (~ 3 m) as reported in Table 2 and Table 4.

Finally, it is important to stress that the years for the collection and generation of the two key inputs for the WSF 3D production – the WSF-IMP, used to outline the human settlement area, and the TDX-DEM employed to estimate the height of the building structures within the built-up area outlined by the WSF-IMP – vary by around seven years. The WSF-IMP input data was collected between 2017 and 2019, the one for the TDX-DEM data between 2011 and 2013. Hence, for settlement areas constructed after 2012, no height information is available in the TDX-DEM. Consequently, the corresponding settlement regions only show valid information for the building fraction (BF), whereas the building height BH exhibits a value of 0.0. Hence, the building volume BV, derived from a combination of BF and BH, is underestimated in these cases as well. However, if required, the user can identify (and remove) the related areas, for instance by excluding all pixels from the WSF 3D settlement area where BH (or the 3 * 3 mean of BH) equals 0.0. Here, it is important to note that the reported accuracies already include the loss of precision due to this effect.

5. Conclusions and outlook

The WSF 3D represents the first globally consistent and complete dataset characterizing the three-dimensional morphology and density of the building stock within all human settlements worldwide. Therewith, the WSF 3D opens up new opportunities for scientific research, but also for the practice of planners, decision makers, and political leaders. This applies, in particular, to the fields of spatial planning, sustainable development, urban climate, urban economics, or disaster and risk management. At the same time, concise data on the building density is essential for an improved modeling and assessment of population distribution, air pollution and emissions, carbon footprint, energy demand, and traffic patterns. Here, the WSF 3D layers, and knowledge gained from them, can help answering key questions and addressing future challenges related to a sustainable and resilient development of the built environment. Despite the limitations of the presented approach to accurately map high-rise building structures, first comprehensive applications of the data have clearly indicated their usefulness. The WSF 3D has, for instance, already been employed (Palacios-Lopez et al., 2019) successfully by the World Bank to predict COVID-19 contagion risk hotspots in African, Asian, and South American cities (Bhardwaj et al., 2020), to forecast combined effects of economic drivers and policy choices on a city's development path (Lall et al., 2021), and to support various national urbanization reviews in Africa and Central America. Moreover, the Asian Development Bank has employed WSF 3D data to support the calculation of a wellness index for Asia (Asian Development Bank, 2020).

Considering the access to the WSF 3D data, DLR intends to pursue an open and free data policy. However, this intention is subject to German data distribution regulations (SatDSiG) and requires a formal confirmation by the responsible federal office. The corresponding approval process is still ongoing. Hence, the WSF 3D data can currently only be provided on the basis of individual requests (contact: guf@dlr.de). All WSF 3D data for which a clearance is granted in accordance with SatDSiG, shall be made accessible via open data repositories and DLR's EOC Geoservice (https://geoservice.dlr.de) and the Urban Thematic Exploitation Platform (Esch et al., 2018a).

Regarding the future activities, it is planned to address the observed lack of accuracy in the context of high-rise building structures by supplementing the analysis of the TDM-DEM in these regions with additional globally available elevation data such as the 30 m ASTER Global Digital Elevation Model Version 3 (GDEM v3) or the ALOS Global Digital Surface Model ALOS World 3D (30 m AW3D30). In the case of these two alternative datasets, a less pronounced layover or offset of the building tops – and therewith a more appropriate representation of the local building heights – can be expected due to the different acquisition methods and imaging geometries, respectively. At the same time the 30 m spatial resolution should still be detailed enough to enable a sufficient reproduction of the local building structures. Therewith, one can assume a potential improvement compared to the significant underestimation occurring on the basis of an exclusive use of the TDM-DEM. In this context it is worth noting that first tests have confirmed the applicability of the developed methodology to derive building heights and volumes from DEM dataset with resolutions of 0.5–30 m.

From an applied perspective, comprehensive quantitative and

qualitative analyses of the global 3D built-up density and urban morphological structuring will be started soon, in order to provide new empirical evidence related to the horizontal and vertical expansion of human settlements worldwide. Moreover, the currently ongoing development of a new global population layer – the WSF population, introduced by Palacios-Lopez et al. (2019) – will be supported through the integration of the 3D built-up volume provided by the WSF 3D. Finally, the WSF 3D project team already works on follow-on methodologic developments which also allow to map the 3D settlement development over time.

Author statement

T. Esch conceived the idea and coordinated and conceptualized the works.

A. Roth organized the access to the TanDEM-X elevation and amplitude data.

E. Brzoska, J. Zeidler, D. Palacios-Lopez, and A. Metz-Marconcini curated the data.

T. Esch, J. Zeidler, and M. Marconcini developed the methodology.

J. Zeidler, T. Esch., and B. Leutner coded the software and managed the processing.

E. Brzoska and D. Palacios-Lopez conducted the validation.

T. Esch, S. Dech, and A. Roth organized and acquired funding and resources.

T. Esch, J. Zeidler, E. Brzoska prepared the original draft of the manuscript.

All authors contributed to the final review and editing of the manuscript.

Funding

This work was supported by internal funding of the German Aerospace Center (DLR); the European Space Agency [contract no. 4000126100/19/I-EF]; the EU-funded ACP-EU Natural Disaster Risk Reduction Program, managed by the Global Facility for Disaster Reduction and Recovery of the World Bank [contract no. 7194331, contract no. 7196541]; the German Federal Institute for Research on Building, Urban Affairs and Spatial Development within the Federal Office for Building and Regional Planning [reference number 10.08.17.7–18.13]; and the Helmholtz Association [Helmholtz Klima Initiative].

Declaration of Competing Interest

The Authors declare no conflicts of interest.

Acknowledgements

The first fundamental methodological research was conducted with internal funding of the German Aerospace Center (DLR). Moreover, the authors wish to acknowledge the European Space Agency (ESA) that supported the extension of the basic approach to an application for large-scale analysis in the project “Artificial Intelligence for Smart Cities” (contract no. 4000126100/19/I-EF). Key components of the various validation campaigns were co-financed by the EU-funded ACP-EU Natural Disaster Risk Reduction Program, managed by the Global Facility for Disaster Reduction and Recovery (World Bank project “Satellite Monitoring Service of Urbanization in Africa”, contract no. 7194331), the project “Development of a concept for information retrieval about the building stock in Germany with remote sensing”, funded by the German Federal Institute for Research on Building, Urban Affairs and Spatial Development within the Federal Office for Building and Regional Planning (reference number 10.08.17.7-18.13), the World Bank in the framework of the project “Cash For Digital Work Microtasking For 3D Urban Morphology In Africa” (contract no. 7196541), and the Helmholtz Klimainitiative “HI-CAM”. Finally, the authors would like to thank the TerraSAR-X and TanDEM-X Science Teams for providing the global DEM and SAR data used to derive the WSF 3D. We also thank Caroline Gevaert, Edward Charles Anderson, Vivien Deparday, Walker Kosmidou-Bradley, Somik Lall, and Hogeun Park from the World Bank for their substantial support in organizing accurate reference data.

References

Asian Development Bank, 2020. Asian Development Outlook (ADO) 2020 Update: Wellness in Worrying Times. Asian Development Outlook. https://doi.org/10.22617/FLS200256-3. https://www.adb.org/sites/default/files/publication/635666/ado2020-update.pdf (accessed on 25.11.2021).

Bakar, A.H.A., Cheen, K.S., 2013. A framework for assessing the sustainable urban development. Procedia Soc. Behav. Sci. 85, 484–492.

Bhardwaj, G., Esch, T., Lall, S.V., Marconcini, M., Soppelsa, M.E., Wahba, S., 2020. Cities, crowding, and the coronavirus: predicting contagion risk hotspots. World Bank. https://doi.org/10.1596/33648.

Bibri, S.E., Krogstie, J., Kärrholm, M., 2020. Compact city planning and development: emerging practices and strategies for achieving the goals of sustainability. DIBE 4, 100021.

Brown De Colstoun, E.C., Huang, C., Wang, P., Tilton, J.C., Tan, B., Phillips, J., Niemczura, S., Ling, P.-Y., Wolfe, R., 2017. Documentation for the global man-made impervious surface (GMIS) dataset from Landsat. SEDAC. https://doi.org/10.7927/H4JD4TVQ.

Clinton, N., Stuhlmacher, M., Miles, A., Uludere Aragon, N., Wagner, M., Georgescu, M., Herwig, C., Gong, P., 2018. A global geospatial ecosystem services estimate of urban agriculture. Earth’s Future 6, 40–60. https://doi.org/10.1002/2017EF000536.

d’Amour, C.B., Reitsma, F., Baiocchi, G., Barthel, S., Güneralp, B., Erb, K.-H., Haberl, H., Creutzig, F., Seto, K.C., 2017. Future urban land expansion and implications for global croplands. Proc. Natl. Acad. Sci. 114, 8939–8944.

De Reu, J., Bourgeois, J., Bats, M., Zwertvaegher, A., Gelorini, V., De Smedt, P., Chu, W., Antrop, M., De Maeyer, P., Finke, P., 2013. Application of the topographic position index to heterogeneous landscapes. Geomorphology 186, 39–49.

Esch, T., Heldens, W., Hirner, A., Keil, M., Marconcini, M., Roth, A., Zeidler, J., Dech, S., Strano, E., 2017. Breaking new ground in mapping human settlements from space - the global urban footprint. ISPRS J. Photogramm. Remote Sens. 134, 30–42. https://doi.org/10.1016/j.isprsjprs.2017.10.012.

Esch, T., Asamer, H., Bachofer, F., Balhar, J., Boettcher, M., Boissier, E., d’Angelo, P., Gevaert, C.M., Hirner, A., Jupova, K., Kurz, F., Kwarteng, A.Y., Mathot, E., Marconcini, M., Marin, A., Metz-Marconcini, A., Pacini, F., Paganini, M., Permana, H., Soukup, T., Uereyen, S., Small, C., Svaton, V., Zeidler, J.N., 2018a. Digital world meets urban planet - new prospects for evidence-based urban studies arising from joint exploitation of big earth data, information technology and shared knowledge. Int. J. Digit. Earth 13, 136–157. https://doi.org/10.1080/17538947.2018.1548655.

Esch, T., Bachofer, F., Heldens, W., Hirner, A., Marconcini, M., Palacios-Lopez, D., Roth, A., Üreyen, S., Zeidler, J., Dech, S., 2018b. Where we live - a summary of the achievements and planned evolution of the Global Urban Footprint. Remote Sens. 10, 895. https://doi.org/10.3390/rs10060895.

Esch, T., Üreyen, S., Zeidler, J., Metz-Marconcini, A., Hirner, A., Asamer, H., Tum, M., Böttcher, M., Kuchar, S., Svaton, V., 2018c. Exploiting big earth data from space - first experiences with the timescan processing chain. Big Earth Data 2, 36–55. https://doi.org/10.1080/20964471.2018.1433790.

Esch, T., Zeidler, J., Palacios-Lopez, D., Marconcini, M., Roth, A., Mönks, M., Leutner, B., Brzoska, E., Metz-Marconcini, A., Bachofer, F., 2020. Towards a large-scale 3D modeling of the built environment - joint analysis of TanDEM-X, Sentinel-2 and Open Street Map data. Remote Sens. 12, 2391. https://doi.org/10.3390/rs12152391.

Falcone, J.A., 2016. US National Categorical Mapping of Building Heights by Block Group from Shuttle Radar Topography Mission Data: U.S. Geological Survey Data Release. https://doi.org/10.5066/F7W09416.

Florczyk, A.J., Melchiorri, M., Zeidler, J., Corbane, C., Schiavina, M., Freire, S., Sabo, F., Politis, P., Esch, T., Pesaresi, M., 2020. The generalised settlement area: mapping the earth surface in the vicinity of built-up areas. Int. J. Digit. Earth 13, 45–60. https://doi.org/10.1080/17538947.2018.1550121.

Frantz, D., Schug, F., Okujeni, A., Navacchi, C., Wagner, W., van der Linden, S., Hostert, P., 2021. National-scale mapping of building height using Sentinel-1 and Sentinel-2 time series. Remote Sens. Environ. 252, 112128 https://doi.org/10.1016/j.rse.2020.112128.

Frolking, S., Milliman, T., Seto, K.C., Friedl, M.A., 2013. A global fingerprint of macro-scale changes in urban structure from 1999 to 2009. Environ. Res. Lett. 8, 024004 https://doi.org/10.1088/1748-9326/8/2/024004.

GDAL/OGR contributors, 2020. GDAL/OGR Geospatial Data Abstraction Software Library. Open Source Geospatial Foundation. https://gdal.org.

Geiß, C., Leichtle, T., Wurm, M., Pelizari, P.A., Standfuß, I., Zhu, X.X., So, E., Siedentop, S., Esch, T., Taubenböck, H., 2019. Large-area characterization of urban morphology - mapping of built-up height and density using TanDEM-X and Sentinel-2 data. IEEE J. Sel. Top. Appl. Earth Obs. Remote Sens. 12, 2912–2927. https://doi.org/10.1109/JSTARS.2019.2917755.

Global Power Synergy Public Company, 2019. Sustainability Report 2018. Chatuchak, Bangkok. https://www.gpscgroup.com/storage/download/sd-report/20190325-gpsc-sd2018-en.pdf.

Gozgor, G., Kablamaci, B., 2015. What happened to urbanization in the globalization era? An empirical examination for poor emerging countries. Ann. Reg. Sci. 55, 533–553.
Grafakos, S., Gianoli, A., Tsatsou, A., 2016. Towards the development of an integrated sustainability and resilience benefits assessment framework of urban green growth interventions. Sustainability 8, 461. https://doi.org/10.3390/su8050461.
Grimm, N.B., Foster, D., Groffman, P., Grove, J.M., Hopkinson, C.S., Nadelhoffer, K.J., Pataki, D.E., Peters, D.P., 2008. The changing landscape: ecosystem responses to urbanization and pollution across climatic and societal gradients. Front. Ecol. Environ. 6, 264–272. https://doi.org/10.1890/070147.
Hallas, M., 2019. Mapping Africa: how Ecopia. ai and Maxar mapped every building and road in Sub-Saharan Africa using high-resolution satellite imagery. American Geophysical Union, Fall Meeting.
He, C., Liu, Z., Tian, J., Ma, Q., 2014. Urban expansion dynamics and natural habitat loss in China: a multiscale landscape perspective. Glob. Chang. Biol. 20, 2886–2902. https://doi.org/10.1111/gcb.12553.
Lafarge, F., Descombes, X., Zerubia, J., Pierrot-Deseilligny, M., 2008. Structural approach for building reconstruction from a single DSM. IEEE Trans. Pattern Anal. Mach. Intell. 32, 135–147. https://doi.org/10.1109/TPAMI.2008.281.
Lall, S.V., Lebrand, M.S.M., Park, H., Sturm, D.M., Venables, A.J., 2021. Pancakes to Pyramids: City Form to Promote Sustainable Growth. World Bank Group, Washington, D.C.. http://documents.worldbank.org/curated/en/554671622446381555/City-Form-to-Promote-Sustainable-Growth (accessed on 25.11.2021).
Li, M., Koks, E., Taubenböck, H., van Vliet, J., 2020. Continental-scale mapping and analysis of 3D building structure. Remote Sens. Environ. 245, 111859 https://doi.org/10.1016/j.rse.2020.111859.
Lützkendorf, T., Balouktsi, M., 2017. Assessing a sustainable urban development: typology of indicators and sources of information. Procedia Environ. Sci. 38, 546–553.
Mahendra, A., Seto, K.C., 2019. Upward and Outward Growth: Managing Urban Expansion for More Equitable Cities in the Global South. World Resources Report. Washington DC. www.citiesforall.org.
Marconcini, M., 2021. The View from Space - How Cities are Growing. German Remote Sensing Data Center. https://www.dlr.de/content/en/articles/news/2021/04/20211111_the-view-from-space-how-cities-are-growing.html (accessed on 25.11.2021).
Marconcini, M., Metz-Marconcini, A., Üreyen, S., Palacios-Lopez, D., Hanke, W., Bachofer, F., Zeidler, J., Esch, T., Gorelick, N., Kakarla, A., 2020. Outlining where humans live - the world settlement footprint 2015. Sci. Data 7, 1–14.
Marshall, S., Gong, Y., Green, N., 2019. Urban compactness: New geometric interpretations and indicators. In: The Mathematics of Urban Morphology. Springer, pp. 431–456.
Mathews, A.J., Frazier, A.E., Nghiem, S.V., Neumann, G., Zhao, Y., 2019. Satellite scatterometer estimation of urban built-up volume: validation with airborne lidar data. Int. J. Appl. Earth Obs. Geoinf. 77, 100–107.
Microsoft, 2018. Microsoft Building Footprints. https://www.microsoft.com/en-us/maps/building-footprints.
Open Street Map, 2017. Planet Dump. retrieved from. https://planet.osm.org. https://www.openstreetmap.org.
Palacios-Lopez, D., Bachofer, F., Esch, T., Heldens, W., Hirner, A., Marconcini, M., Sorichetta, A., Zeidler, J., Künzer, C., Dech, S., Tatem J., A., Reinartz, P., 2019. New Perspectives for Improved Global Population Mapping arising from the World Settlement Footprint. Sustainability 11 (6056). https://doi.org/10.3390/su11216056.
Qin, J., Fang, C., Wang, Y., Li, G., Wang, S., 2015. Evaluation of three-dimensional urban expansion: a case study of Yangzhou City, Jiangsu Province, China. Chin. Geogr. Sci. 25, 224–236. https://doi.org/10.1007/s11769-014-0728-8.
Román, M.O., Wang, Z., Sun, Q., Kalb, V., Miller, S.D., Molthan, A., Schultz, L., Bell, J., Stokes, E.C., Pandey, B., 2018. NASA's black marble nighttime lights product suite. Remote Sens. Environ. 210, 113–143. https://doi.org/10.1016/j.rse.2018.03.017.
Rosenthal, S.S., Strange, W.C., 2003. Geography, industrial organization, and agglomeration. Rev. Econ. Stat. 85, 377–393.
Röthlisberger, H., 1999. Günstiger bauen: Der wohltemperierte Ratgeber für schlaue Bauherren und solche, die es werden wollen. H. Röthlisberger.
Seto, K.C., Güneralp, B., Hutyra, L.R., 2012. Global forecasts of urban expansion to 2030 and direct impacts on biodiversity and carbon pools. Proc. Natl. Acad. Sci. 109, 16083–16088. https://doi.org/10.1073/pnas.1211658109.
Sirko, W., Kashubin, S., Ritter, M., Annkah, A., Bouchareb, Y.S.E., Dauphin, Y., Keysers, D., Neumann, M., Cisse, M., Quinn, J., 2021. Continental-Scale Building Detection from High Resolution Satellite Imagery. arXiv. https://arxiv.org/abs/2107.12283.
Stewart, I.D., Oke, T.R., 2012. Local climate zones for urban temperature studies. Bull. Am. Meteorol. Soc. 93, 1879–1900. https://doi.org/10.1175/BAMS-D-11-00019.1.
Stewart, I.D., Oke, T.R., Krayenhoff, E.S., 2014. Evaluation of the 'local climate zone'scheme using temperature observations and model simulations. IJCli 34, 1062–1080.
Tiecke, T.G., Liu, X., Zhang, A., Gros, A., Li, N., Yetman, G., Kilic, T., Murray, S., Blankespoor, B., Prydz, E.B., Dang, H.-A.H., 2017. Mapping the World Population One Building at a Time. arXiv. https://arxiv.org/abs/1712.05839.
Tison, C., Tupin, F., Maître, H., 2007. A fusion scheme for joint retrieval of urban height map and classification from high-resolution interferometric SAR images. IEEE Trans. Geosci. Remote Sens. 45, 496–505.
United Nations Department of Economic and Social Affairs Population Division, 2019. World Population Prospects: The Highlights, pp. 1–46. https://population.un.org/wpp/Publications/Files/WPP2019_Highlights.pdf (accessed on 25.11.2021).
United Nations Development Programme, 2016. Sustainable Urbanization Strategy: UNDP's Support to Sustainable, Inclusive and Resilient Cities in Developing World. New York, USA. http://www.undp.org/content/dam/undp/library/Sustainable%20Development/Urbanization/UNDP_Urban-Strategy.pdf.
Williams, K., 2000. Does intensifying cities make them more sustainable?. In: Achieving Sustainable Urban Form. Taylor and Francis Group, pp. 30–45.
Xu, G., Dong, T., Cobbinah, P.B., Jiao, L., Sumari, N.S., Chai, B., Liu, Y., 2019. Urban expansion and form changes across African cities with a global outlook: spatiotemporal analysis of urban land densities. J. Clean. Prod. 224, 802–810. https://doi.org/10.1016/j.jclepro.2019.03.276.
Zhang, W., Li, W., Zhang, C., Ouimet, W.B., 2017. Detecting horizontal and vertical urban growth from medium resolution imagery and its relationships with major socioeconomic factors. Int. J. Remote Sens. 38, 3704–3734. https://doi.org/10.1080/01431161.2017.1302113.
Zink, M., Bachmann, M., Brautigam, B., Fritz, T., Hajnsek, I., Moreira, A., Wessel, B., Krieger, G., 2014. TanDEM-X: the new global DEM takes shape. IEEE Geosci. Remote Sens. Mag. 2, 8–23. https://doi.org/10.1109/MGRS.2014.2318895.